



## Article

# Lithium Vanadium Oxide/Graphene Composite as a Promising Anode for Lithium-Ion Batteries

Leichao Meng<sup>1</sup>, Jianhong Peng<sup>1</sup>, Yi Zhang<sup>2</sup> , Yongfu Cui<sup>1</sup>, Lingyun An<sup>1</sup>, Peng Chen<sup>2,3,\*</sup> and Fan Zhang<sup>4,\*</sup>

<sup>1</sup> Qinghai Provincial Key Laboratory of Nanomaterials and Technology, School of Physics and Electronic Information Engineering, Qinghai Minzu University, Xining 810007, China

<sup>2</sup> School of Energy Sciences and Engineering, Nanjing Tech University, Nanjing 211816, China

<sup>3</sup> School of Materials and Chemical Engineering, Tongren University, Tongren 554300, China

<sup>4</sup> School of Materials Science and Engineering, East China Jiaotong University, Nanchang 330013, China

\* Correspondence: chemp@live.cn (P.C.); zhang\_fan2003@126.com (F.Z.)

**Abstract:** Lithium vanadium oxide ( $\text{Li}_3\text{VO}_4$ , LVO) is a promising anode material for lithium-ion batteries (LIBs) due to its high theoretical capacity ( $394 \text{ mAh g}^{-1}$ ) and safe working potential (0.5–1.0 V vs.  $\text{Li}^+/\text{Li}$ ). However, its electrical conductivity is low which leads to poor electrochemical performance. Graphene (GN) shows excellent electrical conductivity and high specific surface area, holding great promise in improving the electrochemical performance of electrode materials for LIBs. In this paper, LVO was prepared by different methods. SEM results showed the obtained LVO by sol-gel method possesses uniform nanoparticle morphology. Next, LVO/GN composite was synthesized by sol-gel method. The flexible GN could improve the distribution of LVO, forming a high conductive network. Thus, the LVO/GN composite showed outstanding cycling performance and rate performance. The LVO/GN composite can provide a high initial capacity of  $350.2 \text{ mAh g}^{-1}$  at 0.5 C. After 200 cycles, the capacity of LVO/GN composite remains 86.8%. When the current density increased from 0.2 C to 2 C, the capacity of LVO/GN composite only reduced from  $360.4 \text{ mAh g}^{-1}$  to  $250.4 \text{ mAh g}^{-1}$ , demonstrating an excellent performance rate.

**Keywords:** lithium vanadium oxide; graphene; anode; lithium-ion batteries



**Citation:** Meng, L.; Peng, J.; Zhang, Y.; Cui, Y.; An, L.; Chen, P.; Zhang, F. Lithium Vanadium Oxide/Graphene Composite as a Promising Anode for Lithium-Ion Batteries. *Nanomaterials* **2023**, *13*, 43. <https://doi.org/10.3390/nano13010043>

Academic Editor: Carlos Miguel Costa

Received: 1 November 2022

Revised: 12 December 2022

Accepted: 12 December 2022

Published: 22 December 2022



**Copyright:** © 2022 by the authors. Licensee MDPI, Basel, Switzerland. This article is an open access article distributed under the terms and conditions of the Creative Commons Attribution (CC BY) license (<https://creativecommons.org/licenses/by/4.0/>).

## 1. Introduction

In recent decades, traditional fossil energy (coal, oil, natural gas) has been widely exploited and utilized, which bring serve negative impacts on the environment such as air pollution, climate warming and other issues. Moreover, fossil energy sources are not renewable. Therefore, it is essential to developing environmentally friendly, renewable and sustainable green energy (wind, solar, etc.). However, the green energy is not continuous. Energy storage devices play an important role in utilizing green energy [1–6]. Among them, lithium-ion batteries (LIBs) show many advantages such as high energy density, high operating voltage, no memory effect, and being environmentally friendly [7–10]. Thus, LIBs have been widely used in various fields, including portable electronic devices, hybrid vehicles, pure electrical vehicles (EVs), and aerospace.

With the rapid development of EVs, there is an increasing demand for EVs' LIBs electrochemical performance. In general, the electrochemical performance of batteries is related to the electrode active materials' intrinsic properties such as theoretical capacity, electrical conductivity, and volume change during cycling [11–13]. At present, the commercial LIBs' anode active material is graphite which is stable during cycling and low cost. However, its theoretical capacity is low ( $372 \text{ mAh g}^{-1}$ ). In addition, the chemical kinetics of graphite is slow. Moreover, the  $\text{Li}^+$  intercalation potential of graphite is low (0.1 V), which leads to lithium dendrites easily forming during charge and discharge, resulting in irreversible lithium loss and battery safety issues. Therefore, the development of novel anode materials

with high-capacity, safe  $\text{Li}^+$  intercalation potential, and long cycle life such as silicon [14], metal oxide [15], transition metal oxides [16] have attracted more and more attention.

Among various anode materials, lithium vanadium oxide ( $\text{Li}_3\text{VO}_4$ , LVO) is a promising anode material for LIBs due to its high theoretical capacity ( $394 \text{ mAh g}^{-1}$ ) and safe working potential (0.5–1.0 V vs.  $\text{Li}^+/\text{Li}$ ) [17]. However, its electrical conductivity is low which leads to poor electrochemical performance. Combining LVO with high conductive carbon material is an effective method to enhance LVO electrochemical performance. Zhai et al. prepared carbon-coated nanosized LVO (LVO-BMC) through ball-milling route followed by CVD technique [18]. The LVO-BMC showed an initial discharge capacity of  $396 \text{ mAh g}^{-1}$  at  $20 \text{ mA g}^{-1}$ , and maintained  $245 \text{ mAh g}^{-1}$  after 50 cycles with an improved capacity retention of 61.9%. Zhang et al. synthesized carbon encapsulated LVO with core-shell nanostructure in which the carbon was uniformly coated on the LVO [19]. Thus, LVO/C showed enhanced cycling stability (maintain  $401 \text{ mAh g}^{-1}$  at 0.1 C after 50 cycles). Zhao et al. fixed LVO nanoparticles in graphitized porous carbon (HP-LVO/C) [20]. The HP-LVO/C showed significantly improved cycle stability (kept a high-capacity of  $381 \text{ mAh g}^{-1}$  at  $0.2 \text{ A g}^{-1}$  after 100 cycles) because the hierarchically porous carbon can provide fast ion transport path and release the volume change of LVO during cycling.

In this work, we prepared LVO by different methods (solid-phase method, hydrothermal method and sol-gel method). The morphology of LVO was studied to confirm the suitable synthesis method. Next, LVO/GN composite was synthesized by sol-gel method. The flexible GN could inhibit the volume expansion of LVO and enhance the electrical conductivity of the LVO/GN composite. As a result, the LVO/GN composite showed a high initial capacity of  $350.2 \text{ mAh g}^{-1}$  at 0.5 C with a high-capacity retention of 86.8% after 200 cycles, which was higher than that of other researchers' results [18–20]. When the current density increased from 0.2 C to 2 C, the capacity of LVO/GN composite only reduced from  $360.4 \text{ mAh g}^{-1}$  to  $250.4 \text{ mAh g}^{-1}$ , demonstrating excellent rate performance. Our LVO/GN composite provided a promising option for high-performance anode materials for LIBs.

## 2. Experimental

### 2.1. Preparation of LVO

The LVO was synthesized by solid-phase method, hydrothermal method and sol-gel method. In solid-state processes,  $\text{Li}_2\text{CO}_3$  and  $\text{V}_2\text{O}_5$  powders with a mole ratio of 3:1 were ground for 0.5 h. The mixture was put into a muffle furnace and kept at  $600 \text{ }^\circ\text{C}$  for 10 h in air with a heating rate of  $5 \text{ }^\circ\text{C min}^{-1}$ . The obtained white sample was LVO (named as S-LVO). For hydrothermal method,  $\text{LiOH}$  and  $\text{V}_2\text{O}_5$  with a mole ratio of 6:1 were mixed in 100 mL deionized water and then poured into a Teflon-lined stainless-steel autoclave at  $180 \text{ }^\circ\text{C}$  for 20 h in an oven. The obtained sample was LVO (named as H-LVO). The sol-gel processes were as follows:  $\text{Li}_2\text{CO}_3$  and  $\text{V}_2\text{O}_5$  powders with a mole ratio of 3:1 were mixed in 100 mL deionized water. The mixture was dried in an oven at  $90 \text{ }^\circ\text{C}$  for 12 h to obtain the precursor powder. Next, the precursor powder was calcined in a tubular furnace at  $600 \text{ }^\circ\text{C}$  for 10 h under Ar. The obtained sample was LVO (named as G-LVO).

### 2.2. Preparation of LVO/GN Composite

The LVO/GN composite was synthesized by sol-gel method. In this case, 200 mg graphene oxide was added in 500 mL deionized water. Next, 30 mmol  $\text{Li}_2\text{CO}_3$  and 10 mmol  $\text{V}_2\text{O}_5$  were mixed in graphene oxide solution. The mixture was dried in an oven at  $90 \text{ }^\circ\text{C}$  for 12 h to obtain the precursor powder. Next, the precursor powder was calcined in a tubular furnace at  $600 \text{ }^\circ\text{C}$  for 10 h under Ar. The obtained sample was LVO/GN composite. The schematic illustration of LVO/GN composite synthesis is shown in Figure 1.

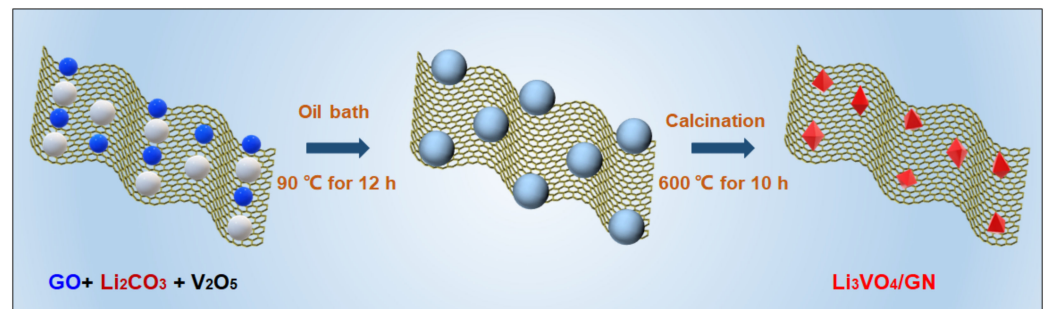


**Figure 1.** Schematic illustration of LVO/GN composite synthesis.

### 2.3. Characterization

The structure of LVO and LVO/GN composite was characterized by X-ray diffraction (XRD, Rigaku MiniFlexII, Rigaku Corporation, Tokyo, Japan). The morphologies of LVO and LVO/GN composite was characterized by scanning electron microscope (SEM, Zeiss Supra 55 and Phenom Prox, Carl Zeiss, Oberkochen, Germany). Thermal gravimetric analysis was performed by a thermal analyzer (TGA, TGA/SDTA 851, Mettler Toledo, Greifensee, Switzerland).

### 2.4. Electrochemical Measurements

In order to prepare anode, we mixed 80% LVO or LVO/GN composite, 10% acetylene black and 10% polyvinylidene fluoride (PVDF) in N-methylpyrrolidone (NMP) to form a slurry which was then coated on copper foil and dried at  $100\text{ }^\circ\text{C}$  for 12 h. The mass loading of active material is about  $1.5\text{ mg cm}^{-2}$ . We assembled it into a CR2025 coin cell in the glove box filled with high-purity Ar, with lithium foil as counter electrode, polypropylene film (Celgard 2400) as separator and 1.0 M  $\text{LiPF}_6$  in ethylene carbonate (EC)/dimethyl carbonate (DMC)/carbon Ethyl methyl acetate (EMC) (in a volume ratio of 1:1:1) with 2% vinylene carbonate (VC) additives as electrolyte. Cyclic voltammetry (CV) and electrochemical impedance spectroscopy (EIS) tests were performed using a CHI660D electrochemical workstation. The cycling performance was tested by a LAND CT2001A battery tester (Wuhan, China).

## 3. Results and Discussion

Figure 2a was the XRD patterns of LVO samples synthesized by solid-phase method, hydrothermal method and sol-gel method. All LVO samples showed peaks at  $2\theta$  of  $16.1^\circ$ ,  $21.6^\circ$ ,  $22.7^\circ$ ,  $24.1^\circ$ ,  $28.0^\circ$ ,  $32.9^\circ$ ,  $36.2^\circ$ ,  $36.4^\circ$ ,  $37.5^\circ$ ,  $40.6^\circ$ ,  $43.1^\circ$ ,  $47.9^\circ$ ,  $50.4^\circ$ ,  $56.7^\circ$ ,  $57.5^\circ$ ,  $58.4^\circ$ ,  $67.1^\circ$ , and  $71.6^\circ$  which were, respectively, attributed to the (100), (110), (011), (101), (111), (200), (210), (002), (201), (112), (211), (221), (202), (230), (300), (320), (203), and (322) diffraction planes of spinel  $\text{Li}_3\text{VO}_4$  (JCPDS No. 38-1247) [21,22]. The crystallite size can be obtained by Debye Scherrer equation  $d = K \lambda / \beta \cos\theta$  in which  $d$  = average crystallite size,  $K$  = the sharp factor,  $\lambda$  = the X-ray wave length,  $\beta$  = the reflection width and  $\theta$  = the diffraction angle [23]. The crystallite sizes of S-LVO, H-LVO, G-LVO calculated from the XRD data were about  $5\text{ }\mu\text{m}$ ,  $3\text{ }\mu\text{m}$ ,  $1\text{ }\mu\text{m}$ . For the XRD diffraction pattern of H-LVO, there were another weak diffraction peaks at about  $30^\circ$ . These peaks are attributed to the (002) and (202) diffraction planes of the  $\text{Li}_2\text{CO}_3$  (JCPDS No. 36-0787) [24]. XRD results show that the purity of LVO sample by hydrothermal method is not high. Hydrothermal synthesis refers to the synthesis through chemical reactions in an aqueous solution above the boiling point of water. The reaction temperature of hydrothermal method is relatively low. Thus, the sample by hydrothermal method is not high purified. The morphologies of three LVO samples were studied to confirm the best synthesis method. Figure 2b is the SEM image of S-LVO (by solid-phase method). It can be seen that S-LVO particle is relatively large ( $2\text{--}10\text{ }\mu\text{m}$ ). In addition, the particle size is various. As shown in Figure 2c, H-LVO particle is also big. However, the particle size is uniform. From Figure 2d, the LVO sample by sol-gel

method showed a relatively small and uniform particle size (1  $\mu\text{m}$ ). From the morphologies of three LVO samples, the sol-gel method is suitable for preparing LVO nanoparticles.

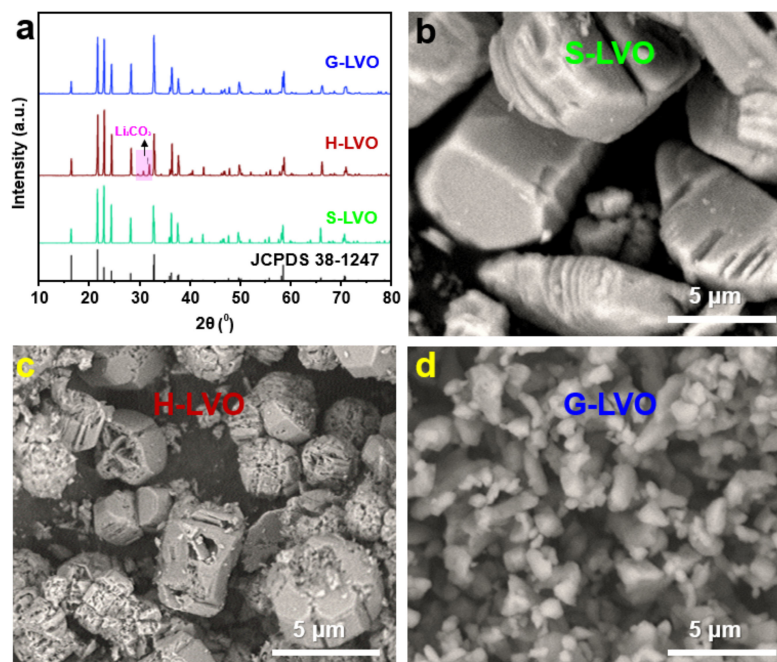


**Figure 2.** (a) XRD patterns of G-LVO, H-LVO, and S-LVO. (b) SEM image of S-LVO. (c) SEM image of H-LVO. (d) SEM image of G-LVO.

According to the analysis above, LVO/GN composite was synthesized by sol-gel method. XRD was carried out to analyze the structure of LVO/GN composite. As shown in Figure 3a, LVO/GN composite showed peaks at  $2\theta$  of  $16.2^\circ$ ,  $21.7^\circ$ ,  $22.8^\circ$ ,  $24.2^\circ$ ,  $28.1^\circ$ ,  $33.0^\circ$ ,  $36.3^\circ$ ,  $36.5^\circ$ ,  $37.6^\circ$ ,  $40.7^\circ$ ,  $43.2^\circ$ ,  $47.9^\circ$ ,  $50.5^\circ$ ,  $56.8^\circ$ ,  $57.6^\circ$ ,  $58.5^\circ$ ,  $67.2^\circ$ , and  $71.7^\circ$  which is similar to that of LVO. The GN's peaks were not observed in XRD pattern of LVO/GN composite, which is due to low GN content in LVO/GN composite. In order to analyze the content of GN, TG experiment of LVO/GN composite was conducted (Figure 3b). From room temperature to  $350^\circ\text{C}$ , the weight loss is 5% which is due to the evaporation of free water on the sample's surface [25–27]. From  $350^\circ\text{C}$  to  $700^\circ\text{C}$ , the weight loss is 11.2% which is the reaction of GN to  $\text{CO}_2$ . When the temperature reached at  $700^\circ\text{C}$ , the weight kept stable. The final product is only LVO. Therefore, the content of GN in the LVO/GN composite is 11.2 wt.%. Figure 3c is the SEM image of LVO/GN composite. Figure 3c showed most LVO nanoparticles uniformly dispersed on GN. Figure 3d is the TEM image of LVO/GN composite. Figure 3d confirmed the uniform distribution of LVO particles on GN. Moreover, the LVO particle size decreased to below 500 nm due to GN inhibiting LVO particle growth. The uniformly dispersed conductive structure can improve the electrical conductivity of LVO/GN composite and buffer the volume expansion of LVO during cycling.

In order to investigate the electrochemical performance of LVO/GN composite, CV experiment was carried out. Figure 4a showed the initial three-cycle CV curves of LVO in the voltage range of 0–3.0 V at a scan rate of  $0.2\text{ mV s}^{-1}$ . The green line is the first cycle. In addition, the red and blue lines are the 2nd and 3rd cycle, respectively. In the first cycle CV curve, three reduction peaks appeared at 0.75 V, 0.62 V and 0.25 V. The peak at 0.25 V could be attributed to the formation of solid electrolyte interface (SEI) film [28–32]. The peaks at 0.75 V and 0.62 V corresponded to  $\text{Li}^+$  intercalation into the LVO. The oxidation peak at 1.35 V indicated that  $\text{Li}^+$  deintercalated from LVO [33,34]. In the subsequent cycles, the reduction peaks changed from 0.75 V and 0.62 V to 0.85 V and 0.72 V while the oxidation peak changed from 1.35 V to 1.32 V. Moreover, the peaks' area increased, which can be attributed to the activation during lithiation and delithiation [35]. For LVO/GN composite,

CV curves were similar to that of pure LVO. However, the current of LVO/GN composite was obviously higher than that of LVO (Figure 4b), implying fast chemical kinetics for LVO/GN composite. Figure 4c showed the galvanostatic charge-discharge curves of the first cycle for LVO/GN electrode at 0.2 C. The galvanostatic charge-discharge curves showed a voltage plateau at 0.85 and 1.35 V, which was consistent with the CV results.

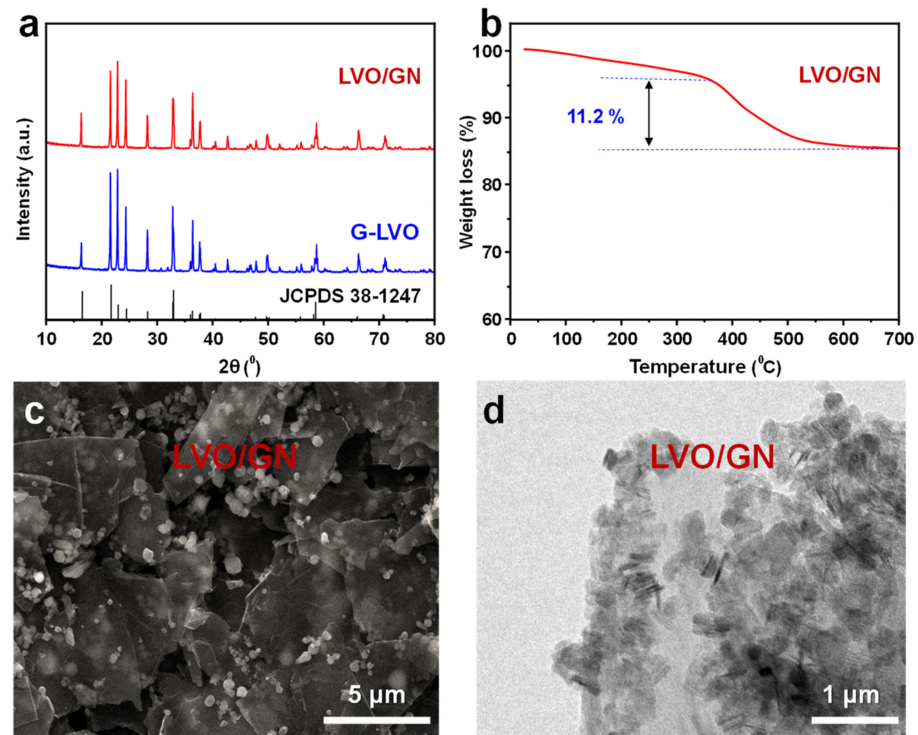


**Figure 3.** (a) XRD patterns of LVO and LVO/GN composite. (b) TGA curve of LVO/GN composite. (c) SEM image of LVO/GN. (d) TEM image of LVO/GN.

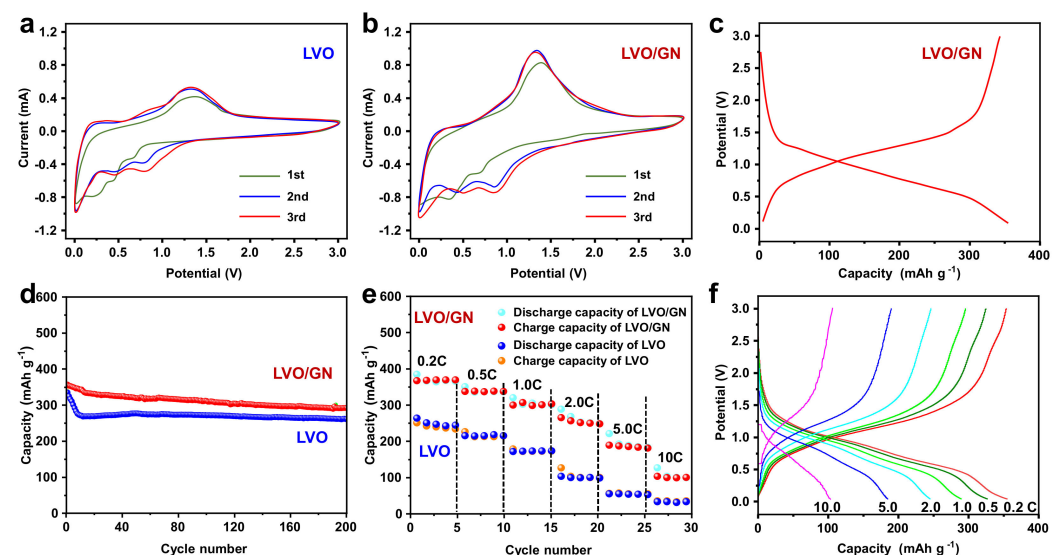


**Figure 4.** (a) CV curves of LVO electrode at a scan rate of  $0.2 \text{ mV s}^{-1}$ . (b) CV curves of LVO/GN electrode at a scan rate of  $0.2 \text{ mV s}^{-1}$ . (c) The charge/discharge curves of LVO/GN electrode at 0.2 C. (d) The cycling performance of LVO electrode and LVO/GN electrode at 0.5 C. (e) The rate performance of LVO electrode and LVO/GN electrode. (f) The charge/discharge curves of LVO/GN electrode at 0.2 C, 0.5 C, 1.0 C, 2.0 C, 5.0 C, 10.0 C. (1 C =  $400 \text{ mA g}^{-1}$ ).

Figure 4d was the cycling performance of LVO and LVO/GN composite. The LVO/GN composite exhibited improved cycling performance. At 0.5 C, the initial reversible capacity of LVO/GN composite was as high as 350.2 mAh g<sup>-1</sup>. After 200 cycles, the capacity was 303.9 mAh g<sup>-1</sup> with a high-capacity retention of 86.8%. For LVO, the capacity fast decreased during the first 15 cycles and slightly increased and then kept stable in the subsequent cycles. This phenomenon was observed in other vanadium oxide [36]. The rapid capacity decrease is resulted from the volume expansion and formation of SEI layer. The capacity's slight increase might then be attributed to the increased crystallinity of active materials and gradual activation progress. The subsequent capacity kept stable due to the complication of activation progress. After 200 cycles, the capacity of LVO was 248.1 mAh g<sup>-1</sup>, and the capacity retention was as low as 71.8%. The capacity was calculated by the total mass of active material in our study. For LVO/GN composite, GN also contributed capacity. At 0.5 C, GN showed a stable capacity of 282.6 mAh g<sup>-1</sup> [37]. We can obtain the capacity of G-LVO in G-LVO/GN composite by the equation:  $Q_{G-LVO/GN} (303.9 \text{ mAh g}^{-1}) = W_{G-LVO} (88.8 \text{ wt\%}) \times Q_{G-LVO} + W_{GN} (11.2 \text{ wt\%}) \times Q_{GN} (282.6 \text{ mAh g}^{-1})$ . The G-LVO in G-LVO/GN composite delivered capacity of 306.8 mAh g<sup>-1</sup> at 0.5 C which is higher than that of pure LVO (248.8 mAh g<sup>-1</sup>). Moreover, LVO/GN composite showed good rate performance (Figure 4e). At 0.2 C, 0.5 C, 1.0 C, 2.0 C, 5.0 C, and 10.0 C, LVO/GN composite showed high discharge capacities of 363.2 mAh g<sup>-1</sup>, 321.3 mAh g<sup>-1</sup>, 301.9 mAh g<sup>-1</sup>, 251.8 mAh g<sup>-1</sup>, 180.5 mAh g<sup>-1</sup>, 100.9 mAh g<sup>-1</sup>, respectively. The charge capacities of LVO/GN composite at 0.2 C, 0.5 C, 1.0 C, 2.0 C, 5.0 C, and 10.0 C were 360.4 mAh g<sup>-1</sup>, 319.8 mAh g<sup>-1</sup>, 300.3 mAh g<sup>-1</sup>, 250.4 mAh g<sup>-1</sup>, 179.6 mAh g<sup>-1</sup>, 100.3 mAh g<sup>-1</sup>, respectively. Under the same rate, the discharge capacities of LVO were only 252.3 mAh g<sup>-1</sup>, 220.6 mAh g<sup>-1</sup>, 180.9 mAh g<sup>-1</sup>, 110.6 mAh g<sup>-1</sup>, 49.9 mAh g<sup>-1</sup>, 40.2 mAh g<sup>-1</sup> while the charge capacities of LVO were only 249.7 mAh g<sup>-1</sup>, 219.8 mAh g<sup>-1</sup>, 180.3 mAh g<sup>-1</sup>, 110.2 mAh g<sup>-1</sup>, 49.8 mAh g<sup>-1</sup>, 40.2 mAh g<sup>-1</sup>, respectively. The galvanostatic charge-discharge curves of the LVO/GN composite at various rates confirm the good rate performance for LVO/GN composite (Figure 4f). The improved electrochemical performance of LVO/GN composite can be attributed to the positive impact of GN and LVO. Compared with commercial graphite anode, LVO/GN composite showed a higher capacity because the theoretical capacity of LVO is higher than that of graphite. Moreover, LVO/GN composite showed better cycling performance than pure LVO. The high mechanical performance of GN could significantly buffer the volume change of LVO during cycling processes, effectively suppressing the electrode pulverization, consequently ensuring the high cyclic stability. GN with high electrical conductivity can increase the electrical conductivity of LVO through offering conductive highways [38,39]. Moreover, small LVO nanoparticles were uniformly distributed on GN to form a multi-dimensional integrated structure, building a comprehensive electron/ion transport network and stable structure, which is beneficial for the cyclic performance [40–42].

In order to characterize the positive effect of GN on LVO, EIS analysis for LVO and LVO/GN composite was carried out. Figure 5a showed the EIS spectrum of LVO and LVO/GN composite. In the EIS spectrum, the high-frequency region is related to the charge transfer process which reveals the characteristics of electrochemical reaction resistance while the low-frequency region is related to the electrical conductivity of electrode material [43–45]. The equivalent circuit model of EIS spectrum is shown in Figure 5b, where R is the interface resistance, R<sub>ct</sub> is the charge transfer resistance, CPE is the capacitance, and W is the Warburg impedance. The R<sub>ct</sub> of LVO/GN composite is smaller than that of LVO electrode, indicating that GN effectively enhances the electrical conductivity of LVO and improves the reaction kinetics.

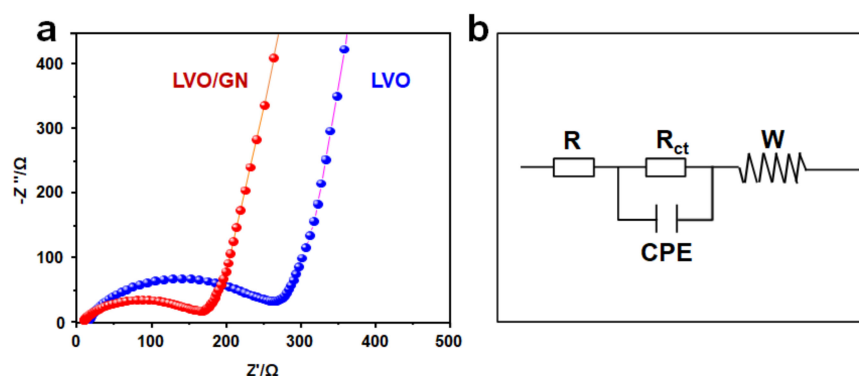


**Figure 5.** (a) Nyquist plots of LVO and LVO/GN. (b) The equivalent circuit model.

#### 4. Conclusions

In conclusion, a high-performance anode material for LIBs was obtained by successfully anchoring LVO nanoparticles uniformly on the GN through a simple sol-gel method. The GN not only improves the ion/electron transport kinetics but also acts as a buffer matrix to effectively alleviate the volume change of LVO during the continuous  $\text{Li}^+$  intercalation/delithiation processes. In addition, LVO nanoparticles were inhibited by GN, which can alleviate the LVO particle growth. As a result, the LVO/GN composite exhibited high reversible capacity ( $350.2 \text{ mAh g}^{-1}$  at  $0.5 \text{ C}$ ), good cyclic performance ( $303.9 \text{ mAh g}^{-1}$  after 200 cycles at  $0.5 \text{ C}$  with a high-capacity retention of 86.8%), and excellent rate capability ( $100.3 \text{ mAh g}^{-1}$  at  $100 \text{ C}$ ). Therefore, the LVO/GN composite is a promising anode material for high-performance LIBs. In addition, the rational design in this work provides a guide for decorating various nanoparticles on the GN, and these materials can be widely used in energy storage, catalysis and other fields.

**Author Contributions:** L.M., writing—original draft; J.P., conceptualization; Y.Z., resources; Y.C., data curation; L.A., conceptualization; P.C., supervision; F.Z., writing—review and editing. All authors have read and agreed to the published version of the manuscript.

**Funding:** This research was funded by the Independent Innovation Fund of Qinghai Minzu University and Tianjin University, the open fund project of Qinghai Provincial Laboratory of Nanomaterials and Nanotechnology, the Foundation of the Department of Science and Technology of the Guizhou province (QKHJC ZK [2022] general 554), Jiangxi Provincial Natural Science Foundation (20212BAB204006) and Jiangxi Province Department of Education Key Science and Technology Research Projects (GJJ190310). And the APC was funded by the Fund of Nanomaterials and Technology Research Team.

**Data Availability Statement:** Not applicable.

**Conflicts of Interest:** The authors declare no conflict of interest.

#### References

- Wang, M.; Liu, X.; Qin, B.; Li, Z.; Zhang, Y.; Yang, W.; Fan, H. In-situ etching and ion exchange induced 2D-2D MXene@ $\text{Co}_9\text{S}_8/\text{CoMo}_2\text{S}_4$  heterostructure for superior  $\text{Na}^+$  storage. *Chem. Eng. J.* **2023**, *451*, 138508. [\[CrossRef\]](#)
- Chen, B.; Wu, W.; Li, C.; Wang, Y.; Zhang, Y.; Fu, L.; Zhu, Y.; Zhang, L.; Wu, Y. Oxygen/phosphorus co-doped porous carbon from cicada slough as high-performance electrode material for supercapacitors. *Sci. Rep.* **2019**, *9*, 5431. [\[CrossRef\]](#) [\[PubMed\]](#)
- Zeng, J.; Bi, L.; Cheng, Y.; Xu, B.; Jen, A.K. Self-assembled monolayer enabling improved buried interfaces in blade-coated perovskite solar cells for high efficiency and stability. *Nano Res. Energy* **2022**, *1*, e9120004. [\[CrossRef\]](#)
- Wang, C.; Wang, Z.; Zhao, D.; Ren, J.; Liu, S.; Tang, H.; Xu, P.; Gao, F.; Yue, X.; Yang, H.; et al. Core-shell  $\text{Co}_2\text{VO}_4$ /carbon composite anode for highly stable and fast-charging sodium-ion batteries. *ACS Appl. Mater. Interfaces* **2021**, *13*, 55020–55028. [\[CrossRef\]](#)
- Gao, F.; Mei, B.; Xu, X.; Ren, J.; Zhao, D.; Zhang, Z.; Wang, Z.; Wu, Y.; Liu, X.; Zhang, Y. Rational design of  $\text{ZnMn}_2\text{O}_4$  nanoparticles on carbon nanotubes for high-rate and durable aqueous zinc-ion batteries. *Chem. Eng. J.* **2022**, *448*, 137742. [\[CrossRef\]](#)
- Zeng, L.; Fang, Y.; Xu, L.; Zheng, C.; Yang, M.; He, J.; Xue, H.; Qian, Q.; Wei, M.; Chen, Q. Rational design of few-layer  $\text{MoSe}_2$  confined within  $\text{ZnSe-C}$  hollow porous spheres for high-performance lithium-ion and sodium-ion batteries. *Nanoscale* **2019**, *11*, 6766–6775. [\[CrossRef\]](#)

7. Liu, X.; Xu, F.; Li, Z.; Liu, Z.; Yang, W.; Zhang, Y.; Fan, H.; Yang, H.Y. Design strategy for MXene and metal chalcogenides/oxides hybrids for supercapacitors, secondary batteries and electro/photocatalysis. *Coord. Chem. Rev.* **2022**, *464*, 214544. [[CrossRef](#)]
8. Zhao, D.; Zhang, Z.; Ren, J.; Xu, Y.; Xu, X.; Zhou, J.; Gao, F.; Tang, H.; Liu, S.; Wang, Z.; et al. Fe<sub>2</sub>VO<sub>4</sub> nanoparticles on rGO as anode material for high-rate and durable lithium and sodium ion batteries. *Chem. Eng. J.* **2023**, *451*, 138882. [[CrossRef](#)]
9. Cai, Z.; Peng, Z.; Wang, M.; Wu, J.; Fan, H.; Zhang, Y. High-pseudocapacitance of porous and square NiO@NC nanosheets for high-performance lithium-ion batteries. *Rare Met.* **2021**, *40*, 1451–1458. [[CrossRef](#)]
10. Zhang, Y.; Wang, Z.; Hu, K.; Ren, J.; Yu, N.; Liu, X.; Wu, G.; Liu, N. Anchoring silicon on the basal plane of graphite via a three-phase heterostructure for highly reversible lithium storage. *Energy Storage Mater.* **2021**, *34*, 311–319. [[CrossRef](#)]
11. Zhao, D.; Jiang, S.; Yu, S.; Ren, J.; Zhang, Z.; Liu, S.; Liu, X.; Wang, Z.; Wu, Y.; Zhang, Y. Lychee seed-derived microporous carbon for high-performance sodium-sulfur batteries. *Carbon* **2023**, *201*, 864. [[CrossRef](#)]
12. Deng, W.; Li, Y.; Xu, D.; Zhou, W.; Xiang, K.; Chen, H. Three-dimensional hierarchically porous nitrogen-doped carbon from water hyacinth as selenium host for high-performance lithium–selenium batteries. *Rare Met.* **2022**, *41*, 3432–3445. [[CrossRef](#)]
13. Pei, C.; Li, T.; Zhang, M.; Wang, J.; Chang, L.; Xiong, X.; Chen, W.; Huang, G.; Han, D. Synergistic effects of interface coupling and defect sites in WO<sub>3</sub>/InVO<sub>4</sub> architectures for highly efficient nitrogen photofixation. *Sep. Purif. Technol.* **2022**, *290*, 120875. [[CrossRef](#)]
14. Jiang, M.; Mu, P.; Zhang, H.; Dong, T.; Tang, B.; Qiu, H.; Chen, Z.; Cui, G. An endotenon sheath-inspired double-network binder enables superior cycling performance of silicon electrodes. *Nano-Micro Lett.* **2022**, *14*, 87. [[CrossRef](#)]
15. Zhang, Y.; Zhang, Y.; Aldama, E.; Liu, H.; Sun, Z.; Ma, Y.; Liu, N.; Zhang, Z. Rational design of walnut-like ZnO/Co<sub>3</sub>O<sub>4</sub> porous nanospheres with substantially enhanced lithium storage performance. *Nanoscale* **2022**, *14*, 166–174. [[CrossRef](#)]
16. Ren, J.; Wang, Z.; Xu, P.; Wang, C.; Gao, F.; Zhao, D.; Liu, S.; Yang, H.; Wang, D.; Niu, C.; et al. Porous Co<sub>2</sub>VO<sub>4</sub> nanodisk as a high-energy and fast-charging anode for lithium-ion batteries. *Nano-Micro Lett.* **2022**, *14*, 5. [[CrossRef](#)]
17. Shi, Y.; Zhang, Y.; Liu, L.; Zhang, Z.; Wang, J.; Chou, S.; Gao, J.; Abruña, H.D.; Li, H.; Liu, H.; et al. Rapid hydrothermal synthesis of Li<sub>3</sub>VO<sub>4</sub> with different favored facets. *J. Solid State Electrochem.* **2017**, *21*, 2547–2553. [[CrossRef](#)]
18. Shao, G.; Gan, L.; Ma, Y.; Li, H.; Zhai, T. Enhancing the performance of Li<sub>3</sub>VO<sub>4</sub> by combining nanotechnology and surface carbon coating for lithium ion batteries. *J. Mater. Chem. A* **2015**, *3*, 11253–11260. [[CrossRef](#)]
19. Zhang, C.; Song, H.; Liu, C.; Liu, Y.; Zhang, C.; Nan, X.; Cao, G. Fast and reversible Li ion insertion in carbon-encapsulated Li<sub>3</sub>VO<sub>4</sub> as anode for lithium-ion battery. *Adv. Funct. Mater.* **2015**, *25*, 3497–3504. [[CrossRef](#)]
20. Zhao, D.; Cao, M. Constructing highly graphitized carbon-wrapped Li<sub>3</sub>VO<sub>4</sub> nanoparticles with hierarchically porous structure as a long life and high capacity anode for lithium-ion batteries. *ACS Appl. Mater. Interfaces* **2015**, *7*, 25084–25093. [[CrossRef](#)]
21. Huang, Y.; Yang, H.; Zhang, Y.; Zhang, Y.; Wu, Y.; Tian, M.; Chen, P.; Trout, R.; Ma, Y.; Wu, T.; et al. A safe and fast-charging lithium-ion battery anode using MXene supported Li<sub>3</sub>VO<sub>4</sub>. *J. Mater. Chem. A* **2019**, *7*, 11250–11256. [[CrossRef](#)]
22. Zhu, L.; Li, Z.; Ding, G.; Xie, L.; Miao, Y.; Cao, X. Review on the recent development of Li<sub>3</sub>VO<sub>4</sub> as anode materials for lithium-ion batteries. *J. Mater. Sci. Technol.* **2021**, *89*, 68–87. [[CrossRef](#)]
23. Zhao, M.; Li, X.; Chen, X.; Li, B.; Kaskel, S.; Zhang, Q.; Huang, J. Promoting the sulfur redox kinetics by mixed organodiselenides in high-energy-density lithium-sulfur batteries. *eScience* **2021**, *1*, 44–52. [[CrossRef](#)]
24. Cai, W.; Chen, R.; Yang, Y.; Yi, M.; Xiang, L. Removal of SO<sub>4</sub><sup>2-</sup> from Li<sub>2</sub>CO<sub>3</sub> by recrystallization in Na<sub>2</sub>CO<sub>3</sub> solution. *Crystals* **2018**, *8*, 19. [[CrossRef](#)]
25. Yao, T.; Zhou, W.; Peng, W.; Zhou, J.; Li, T.; Wu, H.; Zheng, J.; Lin, N.; Liu, D.; Hou, C. Insights into concomitant enhancements of dielectric properties and thermal conductivity of PVDF composites filled with core@double-shell structured Zn@ZnO@PS particles. *J. Appl. Polym. Sci.* **2022**, *139*, e53069. [[CrossRef](#)]
26. Ran, H.; Du, H.; Ma, C.; Zhao, Y.; Feng, D.; Xu, H. Effects of A/B-site Co-doping on microstructure and dielectric thermal stability of AgNbO<sub>3</sub> ceramics. *Sci. Adv. Mater.* **2021**, *13*, 741–747. [[CrossRef](#)]
27. Peng, W.; Zhou, W.; Li, T.; Zhou, J.; Yao, T.; Wu, H.; Zhao, X.; Luo, J.; Liu, J.; Zhang, D. Towards inhibiting conductivity of Mo/PVDF composites through building MoO<sub>3</sub> shell as an interlayer for enhanced dielectric properties. *J. Mater. Sci. Mater. Electron.* **2022**, *33*, 14735–14753. [[CrossRef](#)]
28. Zhang, S.; Sun, L.; Fan, Q.; Zhang, F.; Wang, Z.; Zou, J.; Zhao, S.; Mao, J.; Guo, Z. Challenges and prospects of lithium-CO<sub>2</sub> batteries. *Nano Res. Energy* **2022**, *1*, e9120001. [[CrossRef](#)]
29. Jiang, Y.; Chai, L.; Zhang, D.; Ouyang, F.; Zhou, X.; Alhassan, S.I.; Liu, S.; He, Y.; Yan, L.; Wang, H.; et al. Facet-controlled LiMn<sub>2</sub>O<sub>4</sub>/C as deionization electrode with enhanced stability and high desalination performance. *Nano-Micro Lett.* **2022**, *14*, 176. [[CrossRef](#)]
30. Li, X.; Liang, H.; Liu, X.; Sun, R.; Qin, Z.; Fan, H.; Zhang, Y. Ion-exchange strategy of CoS<sub>2</sub>/Sb<sub>2</sub>S<sub>3</sub> hetero-structured nanocrystals encapsulated into 3D interpenetrating dual-carbon framework for high-performance Na<sup>+</sup>/K<sup>+</sup> batteries. *Chem. Eng. J.* **2021**, *425*, 130657. [[CrossRef](#)]
31. Jia, X.; Yu, X.; Lu, B. Fe<sub>0.8</sub>CoSe<sub>2</sub> nanosphere coated by N-doped carbon for ultra-high rate potassium selenium battery. *Rare Met.* **2021**, *40*, 2455–2463. [[CrossRef](#)]
32. Wang, L.; Qiu, J.; Wang, X.; Chen, L.; Cao, G.; Wang, J.; Zhang, H.; He, X. Insights for understanding multiscale degradation of LiFePO<sub>4</sub> cathodes. *eScience* **2022**, *2*, 125–137. [[CrossRef](#)]
33. Zhang, M.; Bai, R.; King, S.; Yin, F.; Peng, H.; Wang, G. Dual active and kinetically inter-promoting Li<sub>3</sub>VO<sub>4</sub>/graphene anode enabling printable high energy density lithium ion micro capacitors. *Energy Storage Mater.* **2021**, *43*, 482–491. [[CrossRef](#)]
34. Gou, W.; Zhou, S.; Cao, X.; Luo, Y.; Kong, X.; Chen, J.; Xie, X.; Pan, A. Agitation drying synthesis of porous carbon supported Li<sub>3</sub>VO<sub>4</sub> as advanced anode material for lithium-ion batteries. *Rare Met.* **2021**, *40*, 3466–3476. [[CrossRef](#)]

35. Wang, D.; Zhou, C.; Cao, B.; Xu, Y.; Zhang, D.; Li, A.; Zhou, J.; Ma, Z.; Chen, X.; Song, H. One-step synthesis of spherical Si/C composites with onion-like buffer structure as high-performance anodes for lithium-ion batteries. *Energy Storage Mater.* **2020**, *24*, 312–318. [[CrossRef](#)]
36. Lu, S.; Zhu, T.; Li, Z.; Pang, Y.; Shi, L.; Ding, S.; Gao, G. Ordered mesoporous carbon supported Ni<sub>3</sub>V<sub>2</sub>O<sub>8</sub> composites for lithium-ion batteries with long-term and high-rate performance. *J. Mater. Chem. A* **2018**, *6*, 7005–7013. [[CrossRef](#)]
37. Kim, J.; Jeghan, S.; Lee, G. Superior fast-charging capability of graphite anode via facile surface treatment for lithium-ion batteries. *Microporous Mesoporous Mater.* **2020**, *305*, 110325. [[CrossRef](#)]
38. Yang, H.; Zhao, Z.; Yang, Y.; Zhang, Z.; Chen, W.; Yan, R.; Jin, Y.; Zhang, J. Defective WO<sub>3</sub> nanoplates controllably decorated with MIL-101(Fe) nanoparticles to efficiently remove tetracycline hydrochloride by S-scheme mechanism. *Sep. Purif. Technol.* **2022**, *300*, 121846. [[CrossRef](#)]
39. Su, D.; Pei, Y.; Liu, L.; Liu, Z.; Liu, J.; Yang, M.; Wen, J.; Dai, J.; Deng, H.; Cao, G. Wire-in-Wire TiO<sub>2</sub>/C Nanofibers Free-Standing Anodes for Li-Ion and K-Ion Batteries with Long Cycling Stability and High Capacity. *Nano-Micro Lett.* **2021**, *13*, 107. [[CrossRef](#)]
40. Zhou, W.; Cao, G.; Yuan, M.; Zhong, S.; Wang, Y.; Liu, X.; Cao, D.; Peng, W.; Liu, J.; Wang, G.; et al. Core-shell engineering of conductive fillers toward enhanced dielectric properties: A universal polarization mechanism in polymer conductor composites. *Adv. Mater.* **2022**, 2207829. [[CrossRef](#)]
41. Bo, R.; Zhang, F.; Bu, S.; Nasiri, N.; Di Bernardo, I.; Tran-Phu, T.; Shrestha, A.; Chen, H.; Taheri, M.; Qi, S.; et al. One-step synthesis of porous transparent conductive oxides by hierarchical self-assembly of aluminum-doped ZnO nanoparticles. *ACS Appl. Mater. Interfaces* **2020**, *12*, 9589–9599. [[CrossRef](#)] [[PubMed](#)]
42. Zhao, D.; Ge-Zhang, S.; Zhang, Z.; Tang, H.; Xu, Y.; Gao, F.; Liu, S.; Zhou, J.; Wang, Z.; Wu, Y.; et al. Three-Dimensional Honeycomb-Like Carbon as Sulfur Host for Sodium–Sulfur Batteries without the Shuttle Effect. *ACS Appl. Mater. Interfaces* **2022**, *14*, 54662–54669. [[CrossRef](#)] [[PubMed](#)]
43. Liu, Q.; Hu, Y.; Yu, X.; Qin, Y.; Meng, T.; Hu, X. The pursuit of commercial silicon-based microparticle anodes for advanced lithium-ion batteries: A review. *Nano Res. Energy* **2022**, *1*, e9120037. [[CrossRef](#)]
44. Luo, F.; Feng, X.; Zeng, L.; Lin, L.; Li, X.; Kang, B.; Xiao, L.; Chen, Q.; Wei, M.; Qian, Q. In situ simultaneous encapsulation of defective MoS<sub>2</sub> nanolayers and sulfur nanodots into SPAN fibers for high rate sodium-ion batteries. *Chem. Eng. J.* **2021**, *404*, 126430. [[CrossRef](#)]
45. Lin, C.; Yang, X.; Xiong, P.; Lin, H.; He, L.; Yao, Q.; Wei, M.; Qian, Q.; Chen, Q.; Zeng, L. High-rate, large capacity, and long life dendrite-free Zn metal anode enabled by trifunctional electrolyte additive with a wide temperature range. *Adv. Sci.* **2022**, *9*, 2201433. [[CrossRef](#)]

**Disclaimer/Publisher’s Note:** The statements, opinions and data contained in all publications are solely those of the individual author(s) and contributor(s) and not of MDPI and/or the editor(s). MDPI and/or the editor(s) disclaim responsibility for any injury to people or property resulting from any ideas, methods, instructions or products referred to in the content.